

Performance of high impedance resonators in dirty dielectric environments

J. H. Ungerer,^{1,2} D. Sarmah,¹ A. Kononov,¹ J. Ridderbos,^{1,*} R. Haller,¹ L. Y. Cheung,¹ and C. Schönenberger^{1,2,†}

¹*Department of Physics, University of Basel, Klingelbergstrasse 82 CH-4056, Switzerland*

²*Swiss Nanoscience Institute, University of Basel, Klingelbergstrasse 82 CH-4056, Switzerland*

(Dated: September 11, 2023)

High-impedance resonators are a promising contender for realizing long-distance entangling gates between spin qubits. Often, the fabrication of spin qubits relies on the use of gate dielectrics which are detrimental to the quality of the resonator. Here, we investigate loss mechanisms of high-impedance NbTiN resonators in the vicinity of thermally grown SiO₂ and Al₂O₃ fabricated by atomic layer deposition. We benchmark the resonator performance in elevated magnetic fields and at elevated temperatures and find that the internal quality factors are limited by the coupling between the resonator and two-level systems of the employed oxides. Nonetheless, the internal quality factors of high-impedance resonators exceed 10³ in all investigated oxide configurations which implies that the dielectric configuration would not limit the performance of resonators integrated in a spin-qubit device. Because these oxides are commonly used for spin qubit device fabrication, our results allow for straightforward integration of high-impedance resonators into spin-based quantum processors. Hence, these experiments pave the way for large-scale, spin-based quantum computers.

I. INTRODUCTION

Understanding the origin of dielectric losses is crucial when exploiting superconducting resonators for quantum information science. But studies of dielectric losses in various dielectrics have so far been based on low-impedance resonators [1–9]. However, a large resonator impedance is desirable, in-particular in the context of spin-qubits, as the coupling to a weak electric dipole moment scales with the square root of the impedance [10]. Previous studies showed that high-impedance resonators in a clean electrostatic environment typically reach quality factors on the order of 10⁵ [11–14] in the absence of dielectrics.

In applications involving semiconductor qubits, the quality factors of high-impedance resonators are typically limited to $\sim 10^3$ due to gate leakage [15, 16]. Despite these relatively low quality factors, high-impedance resonators have realized important breakthroughs such as coherent coupling between a single photon and a single charge qubit [17, 18], coherent spin-photon coupling [19–23] and distant resonant charge-to-charge [24] and spin-to-spin [25] coupling as well as rapid-gate based spin readout [26] and the demonstration of ultrastrong charge-photon coupling [27]. Impressively, the implementation of high-impedance resonators with quality factors of $\sim 10^3$ has enabled distant virtual-photon mediated charge-to-charge [24] and spin-to-spin [28] coupling.

Incorporating high-impedance resonators with dielectrics would allow one to use established fabrication recipes that employ gate dielectrics aiming on electrostatic stability of quantum dot devices. The fact that

the quality factor of a high-impedance resonator, incorporated in a real device, is not limited by dielectric losses therefore raises the following question: To what extent can dielectrics be employed when fabricating resonator devices without limiting the quality factor to $\lesssim 10^3$?

To answer this question, here we investigate high-impedance NbTiN resonators in a variety of dielectric configurations that are commonly used when fabricating double-quantum dots based on semiconductor nanowires [29–33]. We demonstrate that despite a reduction of the resonator quality factors due to the additional dielectrics, their quality is sufficient even in a dielectric configuration ideal for nanowire integration.

We describe the crucial parameters during sputtering of the material and investigate the dominant resonator loss mechanism. A crucial criterion for resonators aiming on coupling to spin qubits is their magnetic-field resilience which can be achieved by employing disordered superconductors with a high critical magnetic field [12, 13, 34–36]. Recently the community has started to operate spin qubits at elevated temperatures [37–39]. Using these arguments as a motivation, we characterize the resonator performance in large magnetic fields up to 5 T and at elevated temperatures.

II. EXPERIMENTAL SETUP

We fabricated a total of 16 NbTiN coplanar waveguide resonators with an impedance of $Z = \sqrt{L/C} \sim 2 \text{ k}\Omega$ distributed on four different chips with differing dielectric configurations. The sample preparation is described in section III. Each chip hosts a feedline with four notch-type, half-wave resonators as shown in Fig. 1a). From left to right, the different wrapping of the feedline results in coupling quality factors between $Q_c \approx 10^3$ and $Q_c \approx 10^5$ (see Table III in the appendix). This large spread of Q_c enables us to investigate the film properties accurately for a large range of internal quality factors Q_i . Resonance

* Current address: NanoElectronics Group, MESA Institute for Nanotechnology, University of Twente, P.O. Box 217, 7500 AE Enschede, The Netherlands

† www.nanoelectronics.unibas.ch

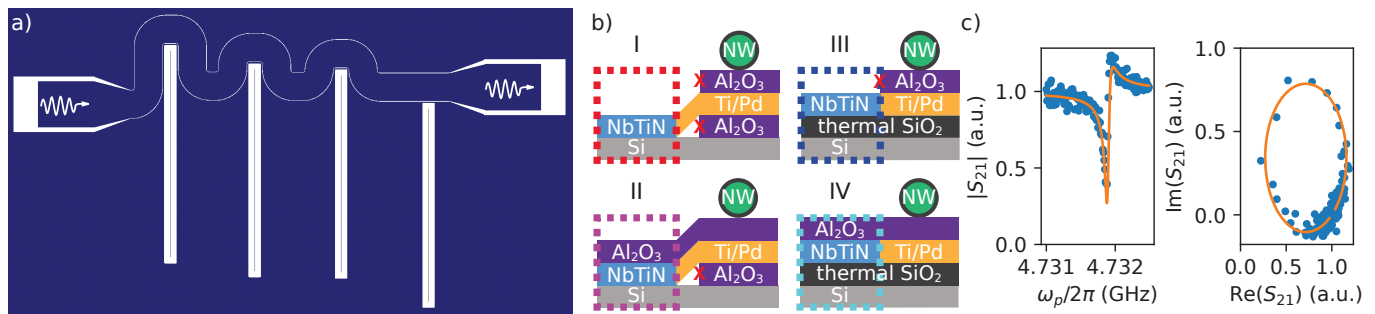


FIG. 1. **Device overview.** a) Top-view design of the four high-impedance ($\sim 2 \text{ k}\Omega$) half-wave resonators, capacitively coupled to a much wider 50Ω matched feedline. b) Side-view schematics of four different dielectric configurations that were investigated. The color of the dashed boxes corresponds to their respective configurations throughout the paper. The right part of each schematic illustrates how a nanowire device can be realized, given the dielectric configuration on its left. c) Amplitude and IQ-excursion of exemplary resonance. The orange line is a fit to the data.

frequencies are in the range between $f_r \sim 4.2 \text{ GHz}$ and $f_r \sim 5.6 \text{ GHz}$.

Fig. 1b) shows the four different dielectric configurations in colored, dashed boxes. For illustrative purposes, the corresponding dielectric configuration of a nanowire device is shown as well and we will explain the advantages and disadvantages of each configuration in the context of nanowire integration below. Case I - NbTiN on Si - is the most ideal configuration for the resonator. But fabricating bottom-gate based devices [33, 40] directly on top of intrinsic silicon comes with the problem of gate leakage, because of the small gate pitch. Moreover, on the surface of the intrinsic silicon, a native silicon oxide forms under ambient conditions which might result in a poor electrostatic device stability. Therefore, fabrication of nanowire devices on top of intrinsic silicon involves sandwiching the bottom gates with two oxide layers grown by atomic-layer deposition (ALD). To maintain a pure dielectric environment of the resonator, the oxide has to be wet-etched or the ALD-layers have to be deposited locally by a lift-off process [41]. Wet-etching of the oxide might lead to unwanted surface-chemistry on the surface of the NbTiN [42]. And, since ALD growth is a conformal processes, the lift-off process might result in irregular, rough edges around the desired structures that may protrude significantly out of plane with respect to the substrate (red crosses in schematic). These edges in turn, may lead to step coverage issues on subsequent metal layers.

The local deposition of oxides for nanowire device integration is alleviated if the whole chip, including the resonator, can be covered with an ALD-grown oxide. We investigate this in case II - Al_2O_3 on NbTiN on Si.

For device integration, it is desirable to work with electrostatically silent oxides. Therefore, nanowire devices are commonly fabricated on top of thermally grown silicon oxide. We therefore investigate the performance of resonators on top of silicon oxide in case III - NbTiN on SiO_2 on Si. In this case bottom-gate based nanowire devices only require one local oxide deposition step as indicated in the schematic. Additionally, the remaining local oxide deposition is alleviated in case IV - Al_2O_3 on

	NbTiN	NbTiN+ Al_2O_3	SiO_2 +NbTiN	SiO_2 +NbTiN+ Al_2O_3
vacuum	0.0963	0.0933	0.1016	0.0947
Al_2O_3 (14 nm)	-	0.0127	-	0.0215
SiO_2 (100 nm)	-	-	0.2035	0.1830
Si (500 μm)	0.9038	0.8940	0.6949	0.7009

TABLE I. **Participation ratios.** Fraction of electric field energy stored in a each dielectric layer for the four investigated films. Values are obtained from performing a dc finite-element simulation using COMSOL.

NbTiN on SiO_2 on Si.

The color codes as introduced in Fig. 1b) are used throughout the rest of the manuscript and denote the dielectric configuration and Tab. I shows the calculated participation ratios of each dielectric for the four investigated dielectric configurations.

III. SAMPLE PREPARATION

Since this work aims to investigate resonator losses due to the choice of the dielectric configuration, the intrinsic Q of the resonators must not be limited by the NbTiN film quality. Here we summarize the steps taken to optimize the fabrication of the used films.

1. As a substrate, we select two undoped Si wafers with a resistivity larger than $10 \text{ k}\Omega\text{cm}$; one with only a layer of native SiO_2 and the other with $\sim 100 \text{ nm}$ of thermally grown SiO_2 .

2. In order to minimize the impurity density at the metal-substrate interface, the wafer with only native oxide undergoes the following etching steps: (i) a Piranha etch to oxidize the top $\sim 10 \text{ nm}$ that may contain contamination, (ii) an HF bath to remove this oxide layer, and (iii) a second Piranha etch, followed by (iv) a second HF bath seconds before loading the wafer into the sputtering chamber. The second wafer hosts $\sim 100 \text{ nm}$ of thermally grown SiO_2 . In order to remove organic residues but keeping the oxide layer intact, we consecutively use ultrasonic cleaning of the wafer in an aqueous solution of

tripotassium orthophosphat [43], distilled water, acetone and isopropanol before loading the wafer into the sputtering chamber.

3. The vacuum quality in the sputtering chamber plays a vital role. We perform Ti pre-sputtering, resulting in a significant reduction of the chamber base pressure.

4. We pre-sputter the NbTi target to remove the top, potentially contaminated or oxidized layer [44].

5. The sputtering rate has to be maximized by choosing an ideal set of sputtering parameters. See Appendix A for details. Because the impingement rates of oxygen and water decreases with increasing growth rates, higher sputtering rates result in a purer film and accordingly lower loss tangents of the resonators [45].

6. We perform sputtering as close as possible to stoichiometry of NbTiN [46]. See Appendix A for details.

7. The resonators are dry-etched using argon/chlorine, offering a higher selectivity against silicon etching compared to the more widely used fluorine based etching recipes [44, 47]. This makes it easier to prevent over-etching. We note that etch-induced losses [47] might limit internal Q factors to $\sim 10^5$, beyond the regime of our interest.

8. After fabrication, each film is characterized in dc measurements by measuring the critical temperature T_c^{dc} and the sheet resistance $R^{\text{sq,dc}}$ close to T_c^{dc} using etched reference structures. This allows us to estimate the sheet kinetic inductance [48–50] which we use to design the resonator geometry. The resonance frequency is designed using analytical equations of coplanar waveguide resonators [51] and the coupling quality factor is estimated by simulating the structure using the electromagnetic simulation software Sonnet.

IV. DETERMINING LOSS DUE TO TWO-LEVEL FLUCTUATORS

To benchmark the performance of the resonators in the different dielectric configurations, we probe each notch-type half-wave resonator by measuring the transmission S_{21} through the feedline at the base temperature of a dilution refrigerator $T_{\text{base}} \approx 30$ mK. Fig. 1c) shows an exemplary resonance which is described by [52, 53]

$$S_{21} = 1 - \frac{Q_l e^{i\Phi}}{Q_c \cos(\Phi)(1 + 2iQ_l(\omega/\omega_r - 1))}. \quad (1)$$

Here $Q_l = 1/(Q_i^{-1} + Q_c^{-1})$ is the loaded quality factor and Φ describes a small resonance asymmetry due to interference with a standing-wave background [52].

We identify 4 resonances on every investigated chip and assign every measured resonance frequency f_r to a physical resonator. Using the physical dimensions of the resonator for calculating its geometric inductance and capacitance [51], we deduce its kinetic inductance from the measured resonance frequency. Thereby, we use the center conductor width which we measure for every resonator by means of scanning electron microscopy after

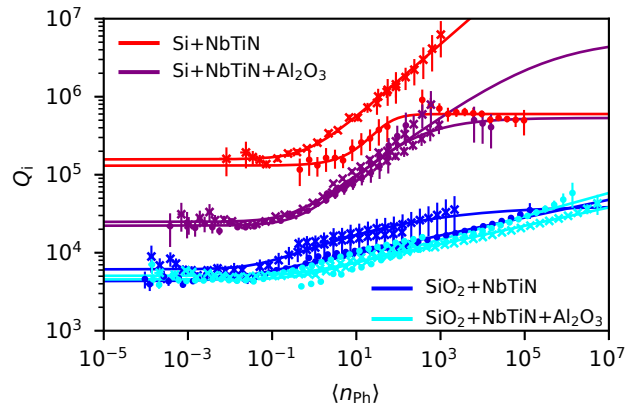


FIG. 2. **Power dependence.** Internal quality factor Q_i as a function of average photon number $\langle n_{\text{ph}} \rangle$ in the resonator. The solid lines are fits to Eq. (3), assuming two level fluctuators as the dominating leakage mechanism at low photon numbers. For each dielectric configuration, as encoded by the color according to Fig. 1b), data for the two resonators with minimal $|Q_{\text{TLS}} - Q_c|$ are plotted. Different symbols correspond to different resonators.

	film A: Si substrate		film B: SiO ₂ substrate	
	NbTiN	NbTiN+Al ₂ O ₃	NbTiN	NbTiN+Al ₂ O ₃
$R^{\text{sq,dc}}$ (Ω)	260 \pm 20		430 \pm 40	
T_c^{dc} (K)	5.8 \pm 0.1		6.6 \pm 0.3	
$L_k^{\text{sq,rf}}$ (pH)	79 \pm 14		61 \pm 9	
D (cm ² /s)	0.27 \pm 0.08		0.32 \pm 0.33	
Q_{TLS}^s (10^3)	152 \pm 9	23.1 \pm 0.9	4.6 \pm 0.3	5.1 \pm 0.2
Q_{other}^s (10^6)	6.3 \pm 0.5	0.63 \pm 0.34	-	-
n_c	0.8 \pm 0.3	0.32 \pm 0.42	0.014 \pm 0.006	0.6 \pm 0.6
β	0.43 \pm 0.04	0.46 \pm 0.29	0.12 \pm 0.02	0.13 \pm 0.02
Q_i^s (10^3)	80 \pm 30	19 \pm 2	3.2 \pm 0.3	2.6 \pm 0.3
Δ_s (mT)	21 \pm 7	66 \pm 8	76 \pm 7	76 \pm 7
g_s	1.98 \pm 0.08	1.94 \pm 0.06	1.782 \pm 0.012	1.72 \pm 0.04

TABLE II. **Resonator properties.** Extracted parameters for the two films with varying dielectric configurations. The sheet resistance $R^{\text{sq,dc}}$ and critical temperature T_c^{dc} are obtained from a dc measurement. The rf sheet kinetic inductance $L_k^{\text{sq,rf}}$ is independently inferred from the 8 measured resonance frequencies of either film, where the error represents the root variance. Q_{TLS} , Q_{other} , n_c and β are fit parameters of Eq. (3). The paramagnetic impurities leading to the feature in Fig. 4a) are characterized by the minimum internal Q-factor Q_i^s and feature width Δ_s . The values of D , Q_{TLS} , Q_{other} , n_c , β , Q_i^s , and Δ_s represent weighted averages over the data sets of 4 resonators of either dielectric configuration with weights proportional to the inverse of the error bar of the fit, resulting in a maximum weight, if $Q_c \sim Q_i$ for which the resonance is most pronounced. g_s is the Landé g-factor extracted from Fig. 4b). The color code corresponds to Fig. 1b).

having performed the experiments presented in this work. The so obtained averaged square kinetic inductance $L_k^{\text{sq,rf}}$ is given in Table II where the error bar represents the root variance. Values for individual resonators are shown in Table III in the appendix. We find that the values of $L_k^{\text{sq,dc}}$ and $L_k^{\text{sq,rf}}$ are consistent for either film.

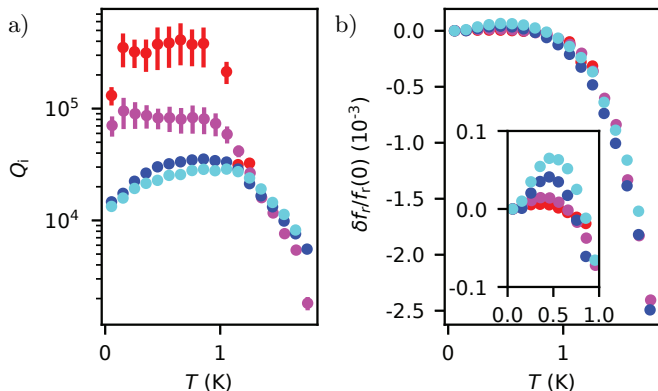


FIG. 3. **Temperature dependence of resonator properties.** a) Internal quality factor Q_i as a function of temperature. b) Relative frequency shift $\delta f_r = (f_r(T) - f_r(0))$ as a function of temperature. The inset is a zoom in onto the peak that is observed at ~ 0.5 K. In all sub-figures, the color encodes the dielectric configuration according to Fig. 1b) and legend in Fig. 2. The data was acquired at an average photon number of $\sim 10^4$.

The differences in $R^{\text{sq,dc}}$ and T_c^{dc} between the two films such as the large variance of $L_k^{\text{sq,rf}}$ is attributed to the small film thickness giving rise to a large effect of film thickness inhomogeneities.

In order to quantify the loss due to two-level systems (TLS) residing in the differing dielectric structures, we measure a resonance trace for every resonator in every dielectric configuration and extract Q_i as a function of power applied on the feedline by fitting Eq. (1) in a circular fit [54]. Fig. 2 shows the fitted internal quality factor Q_i for two resonators of each configuration. We convert the applied power P_{in} on the feedline to an average photon number in the resonator using [13]

$$\langle n_{\text{ph}} \rangle = \frac{Q_c}{\omega_r} \left(\frac{Q_i}{Q_i + Q_c} \right)^2 \frac{P_{\text{in}}}{\hbar\omega_r}, \quad (2)$$

where Q_i , Q_c and ω_r are extracted from fitting the resonance curve. TLS residing in the oxides close to the resonator give rise to a power dependent dielectric loss which is usually modeled by [5, 55–61]

$$\frac{1}{Q_i} = \frac{1}{Q_{\text{TLS}}} \frac{\tanh\left(\frac{\hbar\omega_r}{2k_B T}\right)}{\left(1 + \frac{\langle n_{\text{ph}} \rangle}{n_c}\right)^\beta} + \frac{1}{Q_{\text{other}}}. \quad (3)$$

In the low power limit, and at low temperatures, Q_i is approximately given by Q_{TLS} due to TLS. When increasing $\langle n_{\text{ph}} \rangle$ above a critical value n_c , Q_i increases with a characteristic scaling β until eventually saturating at Q_{other} . We fit Eq. (3) to the data (solid lines in Fig. 2) and extract Q_{TLS} , Q_{other} , n_c and β as fit parameters. The weighted average of these fit parameters for each film are specified in Table III.

We find that Eq. (3) fits well to our data in all four dielectric configurations implying that in the limit of low

photon numbers, all resonators are limited by their coupling to TLS. However, the quantitative behavior for the different dielectric configurations differs by a lot. Let us first consider the low-photon limit in Fig. 2. At low photon numbers, the internal quality factor is determined by the coupling to TLS, $Q_i(n=0) \sim Q_{\text{TLS}}$.

In case I - NbTiN on Si, Q_i saturates at the largest value as the number of photons in the resonator approaches zero. This implies a low abundance of TLS at the interface between the intrinsic silicon and the NbTiN. In case II - Al_2O_3 on NbTiN on Si, Q_i saturates at values approximately an order of magnitude lower which we attribute to the larger abundance of TLS stemming from the ALD-grown oxide on top of the metal and on top of the dielectric. For case III - NbTiN on SiO_2 - and for case IV - Al_2O_3 on NbTiN on SiO_2 , the saturation of Q_i in the low-photon limit happens another order of magnitude lower than for case II. We attribute this decrease to the larger participation ratio (compare Tab. I of the layers below the center conductor compared to the ones above it due to the larger dielectric constant of silicon as compared to the vacuum dielectric constant. The larger importance of the oxides below the center conductor is confirmed by the negligible difference of Q_{TLS} in case III and case IV (with additional oxide on top of the resonator).

In all cases, once the average number of photons $\langle n_{\text{ph}} \rangle$ exceeds a critical value n_c , Q_i increases, because the TLS are increasingly saturated and no longer open a photon leakage path [5, 55, 57, 62].

In the high power limit in case I and case II, all TLS saturate, and Q_i asymptotically approaches Q_{other} which originates from a power independent source of loss. The origin of Q_{other} potentially lies in the interaction with phonons or quasiparticles. In case III and case IV, Q_i does not saturate even at photon numbers on the order of 10^7 underlining the importance of losses due to TLS in these cases.

Despite the TLS being the dominant source of loss for these resonators, we highlight that Q_{TLS} well exceeds 10^3 even for the configuration where the resonator is sandwiched between SiO_2 and Al_2O_3 . This result is a central point of this manuscript as it allows for easier integration of semiconductor nanowires into a resonator architecture maintaining a good resonator quality. Moreover, we stress that Q_{TLS} is larger by almost an order of magnitude when oxides are only grown on top of the metal and not below.

V. RESONATOR STABILITY AT ELEVATED TEMPERATURES AND FIELDS

After having determined the quality of the resonators in each dielectric configuration, quantified by Q_{TLS} , we aim on benchmarking the resonator stability at elevated temperatures and magnetic fields in regimes relevant for spin-qubit operation.

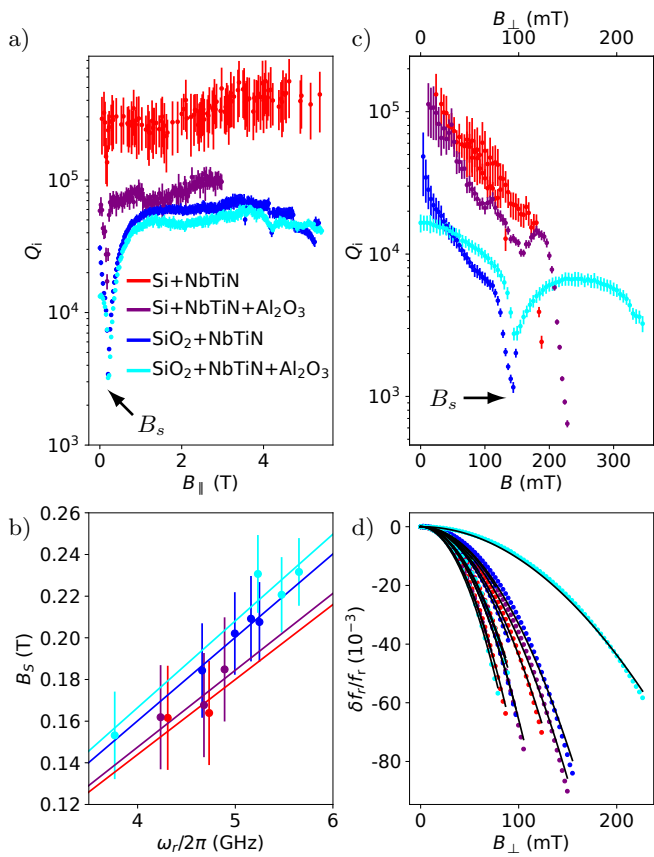


FIG. 4. **Magnetic field dependence** a) Internal quality factor Q_i as a function of in-plane field amplitude B_{\parallel} . A dip is observed at a field B_s which is attributed to resonant paramagnetic impurities. b) B_s extracted from data similar to the one shown in a) for different resonators as a function of resonance frequency ω_r . The solid lines are fits to $B_s = \hbar\omega_r/g_s\mu_B$ from which we extract the Landé g-factor g_s given in Table II. c) Internal quality factor Q_i as a function of out-of-plane field. The field B is applied with an angle of 49° with respect to the substrate and the perpendicular component B_{\perp} is indicated. Once again a dip is observed around $B = \hbar f_r/2\mu_B$, being less pronounced for the resonator fabricated on intrinsic silicon. c) Relative frequency shift $\delta f_r = f_r(B_{\perp}) - f_r(0)$ as a function of out-of-plane field component B_{\perp} . The solid lines are fits to Eq. (4). In all sub-figures, the color encodes the dielectric configuration according to Fig. 1b).

Fig. 3a) shows Q_i as a function of temperature for all dielectric configurations where the color code corresponds to the one introduced in Fig. 1b). For all curves, we measure an increase in Q_i for increasing temperature peaking at ~ 0.8 K. We attribute this increase in the quality factor to an increasing saturation of the TLS with temperature. When the temperature exceeds ~ 1 K, a decline in Q_i is observed which is attributed to an increasing quasiparticle population because of the closing of the superconducting gap [12, 63].

Simultaneously to measuring the quality factor, we also measure the shift in resonance frequency δf_r and plot it

in Fig. 3b). We find that δf_r peaks at a temperature $T_0 \sim 0.5$ K (see inset of figure), with the effect being most pronounced for the resonators fabricated on top of SiO_2 (blue points in Fig. 3). Moreover, the positive frequency shift at increased temperature exceeds the positive frequency shift in the case of TLS saturation due to a large photon population (see Fig. A.2 in the appendix). This effect can be understood by noting that the latter only saturates TLS in a narrow band around the resonance frequency ω_r while the elevated temperature saturates TLS in a much wider frequency range [5]. The temperature of maximum positive frequency shift corresponds to a frequency of $\omega_{\text{thermal}}/2\pi = k_B T_0/h \sim 10$ GHz. As $\omega_{\text{thermal}} > \omega_r$, saturation of TLS in this frequency range explains the positive resonance frequency shift due to the dispersive interaction between resonator and TLS. For larger temperature the resonance frequency starts to decrease due to the closing of the superconducting gap Δ resulting in a larger kinetic inductance, explaining the decrease of δf_r .

In order to benchmark the stability of the NbTiN resonators in an external magnetic field, we plot Q_i as a function of in-plane field B_{\parallel} in Fig. 4a) and as a function of out-of-plane field B_{\perp} in Fig. 4b). During the latter measurement, the magnetic field B was applied with an angle of 49° with respect to the sample plane as indicated by the second longitudinal axis in Fig. 4b). In both cases, we observe a dip in Q_i at an absolute field strength B_s . The dip is attributed to a resonant interaction with paramagnetic impurities in the substrate [12]. Remarkably, the dip is much less pronounced for the resonator fabricated without any additional oxides, indicating that the paramagnetic impurities mainly reside within the oxides. We quantitatively analyze the influence of the paramagnetic impurities by fitting a lorentzian to the dip of each resonator. Therefrom, we extract the minimum quality factor Q_i^s , the feature width Δ_s and the field B_s around which the dip is observed (see Table III in the appendix). Fig. 4(b) shows B_s versus the resonance frequency of the corresponding resonator ω_r . This allows to extract the Landé g-factor g_s by fitting a straight line given by $B_s = \hbar\omega_r/g_s\mu_B$, where μ_B is the Bohr magneton. The resulting values of g_s for the different dielectric configurations are shown in Table II.

Besides this dip-like feature, for the in-plane field, no noteworthy decline in Q_i is observed up to the very largest applied field strengths of 5 T, confirming a magnetic-field resilience for in-plane fields. This is expected because the penetration depth $\lambda \sim 260$ nm [50] is much larger than the thickness of the NbTiN film (~ 10 nm). Out-of-plane, Q_i declines monotonously for increasing field-strengths which we attribute to an increasing quasiparticle density in the film. However, Q_i remains larger than 10^3 up to $B_{\perp} \sim 100$ mT for all dielectric configurations, once again confirming their suitability for spin qubit integration.

Finally, Fig. 4c) shows the resonance frequency versus

out-of-plane field. The data is well fitted by

$$\frac{\delta f_r}{f_r(0)} = -\frac{\pi}{48} \frac{De^2}{\hbar k_B T_c} w^2 B_{\perp}^2 \quad (4)$$

which is deduced from BCS theory [12, 48]. Here, the width w of every resonator center conductor is measured by electron beam microscopy. The average width is $w = 390 \pm 120$ nm where the error bar is the root variance. D denotes the diffusion constant which is a fit parameter.

The weighted average of the fitted diffusion constants are given in Table II and the values for individual resonators are given in Table III. We note that the diffusion constants of the two investigated films are similar and slightly lower than the one in Reference [12].

VI. CONCLUSION

We have investigated superconducting, high-impedance resonators based on NbTiN in four different dielectric configurations. The largest internal quality factor in the low-photon limit is found for the resonator fabricated on intrinsic silicon. Nevertheless, all other dielectric configurations result in internal quality factors $> 10^3$, a value which has proven sufficient for performing

key experiments in the context of spin qubits. Moreover, we benchmark the resonator performance at elevated temperatures and magnetic-field strengths. Since the resonators are compatible with existing fabrication protocols, our results allow for straightforward integration of these types of resonators with various kinds of spin qubits defined in semiconductor nanowires.

We acknowledge very fruitful discussions with Mihai Gabureac, Sergey Amitonov and Alessia Pally. Furthermore, we thank Dario Marty for the support in wafer etching in the facilities of the Paul Scherrer Institute. This research was supported by the Swiss Nanoscience Institute (SNI), the Swiss National Science Foundation through grant 192027 and through the NCCR Spin Qubit in Silicon (NCCR-Spin). We further acknowledge funding from the European Union's Horizon 2020 research and innovation programme, specifically the FET-open project AndQC, agreement No 828948 and the FET-open project TOPSQUAD, agreement No 847471. We also acknowledge support through the Marie Skłodowska-Curie COFUND grant QUSTEC, grant agreement N° 847471 and the Basel Quantum Center through a Georg H. Endress fellowship. All data in this publication are available in numerical form at: <https://doi.org/10.5281/zenodo.7602078>.

-
- [1] J. M. Martinis, K. B. Cooper, R. McDermott, M. Steffen, M. Ansmann, K. Osborn, K. Cicak, S. Oh, D. P. Pappas, R. W. Simmonds, and C. C. Yu, *Physical review letters* **95**, 210503 (2005).
 - [2] A. D. O'Connell, M. Ansmann, R. C. Bialczak, M. Hofheinz, N. Katz, E. Lucero, C. McKenney, M. Neeley, H. Wang, E. M. Weig, A. N. Cleland, and J. M. Martinis, *Applied Physics Letters* **92**, 112903 (2008).
 - [3] J. Gao, M. Daal, A. Vayonakis, S. Kumar, J. Zmuidzinas, B. Sadoulet, B. A. Mazin, P. K. Day, and H. G. Leduc, *Applied Physics Letters* **92**, 152505 (2008).
 - [4] K. Cicak, D. Li, J. A. Strong, M. S. Allman, F. Altomare, A. J. Sirois, J. D. Whittaker, J. D. Teufel, and R. W. Simmonds, *Applied Physics Letters* **96**, 093502 (2010).
 - [5] D. P. Pappas, M. R. Vissers, D. S. Wisbey, J. S. Kline, and J. Gao, *IEEE Transactions on Applied Superconductivity* **21**, 871 (2011).
 - [6] H. Paik and K. D. Osborn, *Applied Physics Letters* **96**, 072505 (2010).
 - [7] C. R. H. McRae, R. Lake, J. Long, M. Bal, X. Wu, B. Jugdersuren, T. Metcalf, X. Liu, and D. P. Pappas, *Applied Physics Letters* **116**, 194003 (2020).
 - [8] M. Müller, T. Luschmann, A. Faltermeier, S. Weichselbaumer, L. Koch, G. B. Huber, H. W. Schumacher, N. Ubbelohde, D. Reifert, T. Scheller, F. Deppe, A. Marx, S. Philipp, M. Althammer, R. Gross, and H. Huebl, *Materials for Quantum Technology* **2**, 015002 (2022).
 - [9] C. R. H. McRae, H. Wang, J. Gao, M. R. Vissers, T. Brecht, A. Dunsworth, D. P. Pappas, and J. Mutus, *Review of Scientific Instruments* **91**, 091101 (2020).
 - [10] A. Blais, R.-S. Huang, A. Wallraff, S. M. Girvin, and R. J. Schoelkopf, *Physical Review A* **69**, 062320 (2004).
 - [11] V. Singh, B. H. Schneider, S. J. Bosman, E. P. Merkkx, and G. A. Steele, *Applied Physics Letters* **105**, 222601 (2014).
 - [12] N. Samkharadze, A. Bruno, P. Scarlino, G. Zheng, D. DiVincenzo, L. DiCarlo, and L. Vandersypen, *Physical Review Applied* **5**, 044004 (2016).
 - [13] C. X. Yu, S. Zihlmann, G. Troncoso Fernández-Bada, J.-L. Thomassin, F. Gustavo, É. Dumur, and R. Maurand, *Applied Physics Letters* **118**, 054001 (2021).
 - [14] L. Grünhaupt, N. Maleeva, S. T. Skacel, M. Calvo, F. Levy-Bertrand, A. V. Ustinov, H. Rotzinger, A. Monfardini, G. Catelani, and I. M. Pop, *Physical review letters* **121**, 117001 (2018).
 - [15] X. Mi, J. Cady, D. Zajac, J. Stehlik, L. Edge, and J. R. Petta, *Applied Physics Letters* **110**, 043502 (2017).
 - [16] P. Harvey-Collard, G. Zheng, J. Dijkema, N. Samkharadze, A. Sammak, G. Scappucci, and L. M. Vandersypen, *Physical Review Applied* **14**, 034025 (2020).
 - [17] A. Stockklauser, P. Scarlino, J. V. Koski, S. Gasparinetti, C. K. Andersen, C. Reichl, W. Wegscheider, T. Ihn, K. Ensslin, and A. Wallraff, *Physical Review X* **7**, 011030 (2017).
 - [18] X. Mi, J. Cady, D. Zajac, P. Deelman, and J. R. Petta, *Science* **355**, 156 (2017).
 - [19] N. Samkharadze, G. Zheng, N. Kalhor, D. Brousse, A. Sammak, U. Mendes, A. Blais, G. Scappucci, and L. Vandersypen, *Science* **359**, 1123 (2018).
 - [20] X. Mi, M. Benito, S. Putz, D. M. Zajac, J. M. Taylor,

- G. Burkard, and J. R. Petta, *Nature* **555**, 599 (2018).
- [21] A. J. Landig, J. V. Koski, P. Scarlino, U. Mendes, A. Blais, C. Reichl, W. Wegscheider, A. Wallraff, K. Ensslin, and T. Ihn, *Nature* **560**, 179 (2018).
- [22] C. X. Yu, S. Zihlmann, J. C. Abadillo-Uriel, V. P. Michal, N. Rambal, H. Niebojewski, T. Bedecarrats, M. Vinet, É. Dumur, M. Filippone, *et al.*, *Nature Nanotechnology*, 1 (2023).
- [23] J. H. Ungerer, A. Pally, A. Kononov, S. Lehmann, J. Ridderbos, C. Thelander, K. A. Dick, V. F. Maisi, P. Scarlino, A. Baumgartner, *et al.*, arXiv preprint arXiv:2303.16825 (2023).
- [24] D. J. van Woerkom, P. Scarlino, J. H. Ungerer, C. Müller, J. V. Koski, A. J. Landig, C. Reichl, W. Wegscheider, T. Ihn, K. Ensslin, and A. Wallraff, *Physical Review X* **8**, 041018 (2018).
- [25] F. Borjans, X. Croot, X. Mi, M. Gullans, and J. Petta, *Nature* **577**, 195 (2020).
- [26] G. Zheng, N. Samkharadze, M. L. Noordam, N. Kalhor, D. Brousse, A. Sammak, G. Scappucci, and L. M. Vandersypen, *Nature nanotechnology* **14**, 742 (2019).
- [27] P. Scarlino, J. H. Ungerer, D. van Woerkom, M. Mancini, P. Stano, C. Muller, A. Landig, J. Koski, C. Reichl, W. Wegscheider, T. Ihn, and A. Wallraff, arXiv preprint arXiv:2104.03045 (2021).
- [28] P. Harvey-Collard, J. Dijkema, G. Zheng, A. Sammak, G. Scappucci, and L. M. Vandersypen, *Physical Review X* **12**, 021026 (2022).
- [29] C. Fasth, A. Fuhrer, M. T. Björk, and L. Samuelson, *Nano letters* **5**, 1487 (2005).
- [30] K. D. Petersson, L. W. McFaul, M. D. Schroer, M. Jung, J. M. Taylor, A. A. Houck, and J. R. Petta, *Nature* **490**, 380 (2012).
- [31] Y. Hu, F. Kuemmeth, C. M. Lieber, and C. M. Marcus, *Nature nanotechnology* **7**, 47 (2012).
- [32] D. Barker, S. Lehmann, L. Namazi, M. Nilsson, C. Thelander, K. A. Dick, and V. F. Maisi, *Applied Physics Letters* **114**, 183502 (2019).
- [33] F. N. Froning, L. C. Camenzind, O. A. van der Molen, A. Li, E. P. Bakkers, D. M. Zumbühl, and F. R. Braakman, *Nature Nanotechnology* **16**, 308 (2021).
- [34] J. Kroll, F. Borsoi, K. Van Der Enden, W. Uilhoorn, D. De Jong, M. Quintero-Pérez, D. Van Woerkom, A. Bruno, S. Plissard, D. Car, E. Bakkers, M. Cassidy, and L. Kouwenhoven, *Physical Review Applied* **11**, 064053 (2019).
- [35] C. W. Zollitsch, J. O'Sullivan, O. Kennedy, G. Dold, and J. J. Morton, *AIP Advances* **9**, 125225 (2019).
- [36] K. Borisov, D. Rieger, P. Winkel, F. Henriques, F. Valenti, A. Ionita, M. Wessbecher, M. Spiecker, D. Gusenkova, I. Pop, and W. Wernsdorfer, *Applied Physics Letters* **117**, 120502 (2020).
- [37] L. Petit, H. Eenink, M. Russ, W. Lawrie, N. Hendrickx, S. Philips, J. Clarke, L. Vandersypen, and M. Veldhorst, *Nature* **580**, 355 (2020).
- [38] C. H. Yang, R. Leon, J. Hwang, A. Saraiva, T. Tantt, W. Huang, J. Camirand Lemyre, K. W. Chan, K. Tan, F. E. Hudson, K. M. Itoh, A. Morello, M. Pioro-Ladrière, A. Laucht, and A. S. Dzurak, *Nature* **580**, 350 (2020).
- [39] L. C. Camenzind, S. Geyer, A. Fuhrer, R. J. Warburton, D. M. Zumbühl, and A. V. Kuhlmann, *Nature Electronics* **5**, 178 (2022).
- [40] F. Froning, M. Rehm, J. Ridderbos, M. Brauns, F. Zwanenburg, A. Li, E. Bakkers, D. Zumbühl, and F. Braakman, *Applied physics letters* **113**, 073102 (2018).
- [41] M. Biercuk, D. Monsma, C. Marcus, J. Becker, and R. Gordon, *Applied Physics Letters* **83**, 2405 (2003).
- [42] E. Toomey, M. Colangelo, N. Abedzadeh, and K. K. Berggren, *Journal of Vacuum Science & Technology B, Nanotechnology and Microelectronics: Materials, Processing, Measurement, and Phenomena* **36**, 06JC01 (2018).
- [43] The used solution has the brand name deconex[®] 12 BA-SIC 2% solution.
- [44] M. R. Vissers, J. Gao, D. S. Wisbey, D. A. Hite, C. C. Tsuei, A. D. Corcoles, M. Steffen, and D. P. Pappas, *Applied Physics Letters* **97**, 232509 (2010).
- [45] Discussion with Mihai Gabureac.
- [46] S. Ohya, B. Chiaro, A. Megrant, C. Neill, R. Barends, Y. Chen, J. Kelly, D. Low, J. Mutus, P. O'Malley, P. Roushan, D. Sank, A. Vainsencher, J. Wenner, T. C. White, Y. Yin, B. D. Schultz, C. J. Palmström, B. A. Mazin, A. N. Cleland, and J. M. Martinis, *Superconductor Science and Technology* **27**, 015009 (2013).
- [47] M. Sandberg, M. R. Vissers, J. S. Kline, M. Weides, J. Gao, D. S. Wisbey, and D. P. Pappas, *Applied Physics Letters* **100**, 262605 (2012).
- [48] M. Tinkham, *Introduction to superconductivity* (Courier Corporation, 2004).
- [49] A. J. Annunziata, D. F. Santavicca, L. Frunzio, G. Catelani, M. J. Rooks, A. Frydman, and D. E. Prober, *Nanotechnology* **21**, 445202 (2010).
- [50] T. Hong, K. Choi, K. Ik Sim, T. Ha, B. Cheol Park, H. Yamamori, and J. Hoon Kim, *Journal of Applied Physics* **114**, 243905 (2013).
- [51] K. Gupta, *Microstrip Lines and Slotlines* (Artech House, Massachusetts, 1990).
- [52] M. S. Khalil, M. Stoutimore, F. Wellstood, and K. Osborn, *Journal of Applied Physics* **111**, 054510 (2012).
- [53] J. Gao, *The physics of superconducting microwave resonators* (California Institute of Technology, 2008).
- [54] S. Probst, F. Song, P. A. Bushev, A. V. Ustinov, and M. Weides, *Review of Scientific Instruments* **86**, 024706 (2015).
- [55] W. A. Phillips, *Reports on Progress in Physics* **50**, 1657 (1987).
- [56] H. Wang, M. Hofheinz, J. Wenner, M. Ansmann, R. Bialczak, M. Lenander, E. Lucero, M. Neeley, A. O'Connell, D. Sank, M. Weides, A. N. Cleland, and J. M. Martinis, *Applied Physics Letters* **95**, 233508 (2009).
- [57] J. Goetz, F. Deppe, M. Haerberlein, F. Wulschner, C. W. Zollitsch, S. Meier, M. Fischer, P. Eder, E. Xie, K. G. Fedorov, E. P. Menzel, A. Marx, and R. Gross, *Journal of Applied Physics* **119**, 015304 (2016).
- [58] J. D. Brehm, A. Bilmes, G. Weiss, A. V. Ustinov, and J. Lisenfeld, *Applied Physics Letters* **111**, 112601 (2017).
- [59] F. W. Carter, T. Khaire, C. Chang, and V. Novosad, *Applied Physics Letters* **115**, 092602 (2019).
- [60] C. Müller, J. H. Cole, and J. Lisenfeld, *Reports on Progress in Physics* **82**, 124501 (2019).
- [61] M. Scigliuzzo, L. E. Bruhat, A. Bengtsson, J. J. Burnett, A. F. Roudsari, and P. Delsing, *New Journal of Physics* **22**, 053027 (2020).
- [62] J. M. Sage, V. Bolkhovskiy, W. D. Oliver, B. Turek, and P. B. Welander, *Journal of Applied Physics* **109**, 063915 (2011).

- [63] P. Coumou, M. Zuiddam, E. Driessen, P. De Visser, J. Baselmans, and T. Klapwijk, IEEE transactions on applied superconductivity **23**, 7500404 (2012).
- [64] D. Glowacka, D. Goldie, S. Withington, H. Muhammad, G. Yassin, and B. Tan, arXiv preprint arXiv:1401.2292 (2014).

Appendix A: Investigation of sputtering parameters

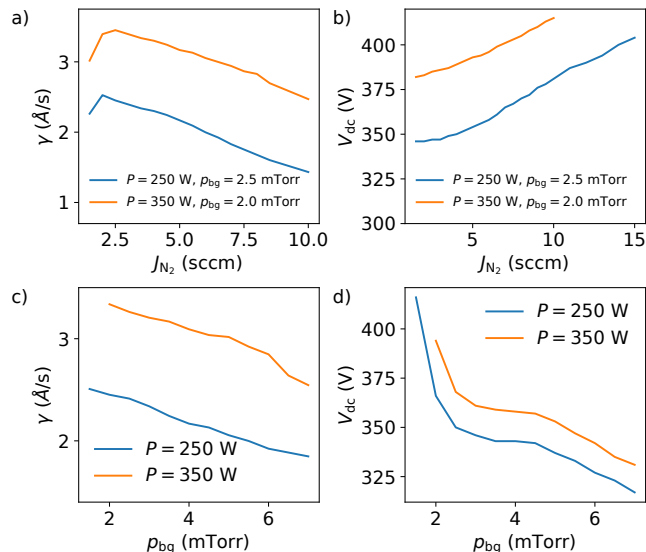


FIG. A.1. **Sputtering parameters.** a) growth rate γ as function of nitrogen flow J_{N_2} at different back-ground pressures ρ_{bg} and plasma power P . b) dc voltage V_{dc} between plasma source and target as function of J_{N_2} for two values of ρ_{bg} and P . A kink in the curve is observed in both a) and b) at the same values of J_{N_2} . This kink corresponds to sputtering at a stoichiometric ratio. c) growth rate γ as a function of background pressure ρ_{bg} showing a monotonous decay as lower ρ_{bg} correspond to larger mean-free paths and therefore to a smaller scattering of the sputtered material. d) dc voltage V_{dc} between the plasma source and the target as a function of background pressure ρ_{bg} . When lowering $\rho_{bg} < 2$ mTorr, V_{dc} increases drastically and the plasma becomes unstable. All traces were measured at a fixed argon flow rate $Q_{Ar} = 50$ sccm.

In this appendix, we give detailed background information about the choice of sputtering parameters that are used while fabricating the resonators as described in Section III in the main text.

In order to minimize the impurity density of the sputtered NbTiN film, it is desirable to maximize the growth rate γ , because a shorter sputtering time results in less gathered contaminants in the film. While sputtering, the plasma power P , the background pressure ρ_{bg} , the argon flow J_{Ar} and the nitrogen flow J_{N_2} can be controlled. In Fig. A.1, we investigate the dependence of the growth rate γ and the voltage between the plasma source and the target V_{dc} on these parameters. The growth rate increases as a function of P . Therefore, the power should be chosen as high as possible while maintaining a stable plasma which is the case in our chamber for $P \lesssim 250$ W. As a function of J_{N_2} , a maximum in the growth rate is found, corresponding to the stoichiometric ratio [64] (see Fig. A.1a) and Fig. A.1b)). The position of the opti-

um depends on P and ρ_{bg} . When increasing ρ_{bg} , γ decreases (see Fig. A.1c)). Therefore, the background pressure should be chosen as small as possible before the plasma becomes unstable. In our sputtering chamber, this is the case for $\rho_{bg} \lesssim 2$ mTorr. We choose $P = 250$ W, $\rho_{bg} = 2$ mTorr, $J_{Ar} = 50$ sccm, $J_{N_2} = 3.5$ sccm for the sputtering of both films.

Appendix B: Frequency shift in power dependence

In the inset of Fig. 3b) in the main text, we observe a substantial positive resonance frequency shift as a function of temperature with a peak at approximately 0.5 K. We attribute this shift to a saturation of TLS with a transition frequency of approximately 10 GHz dispersively interacting with the resonator. Fig. A.2 shows the resonance frequency shift as a function of number of photons in the resonator. The observed positive shift is smaller by an order of magnitude compared to Fig. 3.

For very large drive powers with $\langle n_{ph} \rangle \gtrsim 10^5$, a negative relative frequency shift is observed in Fig. A.2. We attribute this negative shift to the onset of the bifurcation of the resonator due to a finite non-linearity.

ADDITIONAL DATA

All extracted data for each of the 16 individual resonators is shown in Table III.

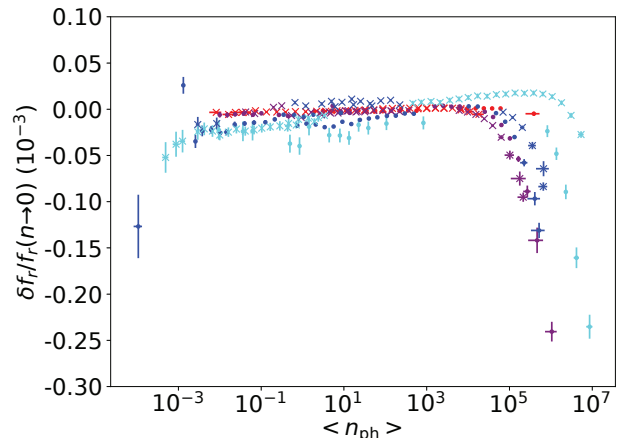


FIG. A.2. **Power dependence.** Relative frequency shift $\delta f_r = f_r - f_r(n \rightarrow 0)$ as function of average number of photons in the resonator $\langle n_{ph} \rangle$. We do not observe a noteworthy positive frequency shift in comparison with the Fig. 3 in the main text. For $\langle n_{ph} \rangle \gtrsim 10^5$, an increasingly negative relative frequency shift is observed which we attribute to the finite non-linearity of the resonators.

	Si + NbTiN			
	resonator #1	resonator #2	resonator #3	resonator #4
f_r (GHz)	4.308	4.728	4.732	4.807
$L_k^{\text{sq,rf}}$ (pH)	93.5	62	77	75
Q_c	(3800 ± 400)	(17000 ± 3000)	(119000 ± 9000)	(400 ± 40)
D (cm ² /s)	0.21	0.39	0.26	0.29
$Q_{\text{TLS}}(10^5)$	-	(1.15 ± 0.24)	(1.6 ± 0.08)	(1.6 ± 1.2)
$Q_{\text{other}}(10^5)$	-	(6.3 ± 0.5)	-	(1.87 ± 0.08)
n_c	-	-	(1.0 ± 0.4)	-
β	-	(1.7 ± 1.5)	(0.49 ± 0.06)	-
$Q_i^S(10^4)$	(4.62 ± 0.08)	-	(9.01 ± 0.04)	-
Δ_S	-	-	(0.021 ± 0.007)	-
	Si+NbTiN+Al ₂ O ₃			
	resonator #5	resonator #6	resonator #7	resonator #8
f_r (GHz)	4.235	4.680	4.891	4.944
$L_k^{\text{sq,rf}}$ (pH)	104	68	80	74
Q_c	(5700 ± 700)	(100000 ± 20000)	(12100 ± 800)	(180 ± 70)
D (cm ² /s)	0.17	0.36	0.21	0.26
$Q_{\text{TLS}}(10^4)$	(2.30 ± 0.12)	(1.87 ± 0.21)	(2.51 ± 0.16)	(5.2 ± 1.0)
$Q_{\text{other}}(10^5)$	(5.3 ± 0.6)	(3.4 ± 2.0)	-	(0.73 ± 0.05)
n_c	(1.1 ± 0.4)	(0.10 ± 0.09)	(0.42 ± 0.23)	-
β	(0.68 ± 0.09)	(0.31 ± 0.08)	(0.42 ± 0.07)	-
$Q_i^S(10^4)$	-	(1.866 ± 0.026)	(3.40 ± 0.04)	-
Δ_S	-	(0.065 ± 0.008)	(0.07 ± 0.018)	-
	Si + SiO ₂ + NbTiN			
	resonator #9	resonator #10	resonator #11	resonator #12
f_r (GHz)	4.660	4.99	5.161	5.247
$L_k^{\text{sq,rf}}$ (pH)	74	53	60	54
Q_c	(10000 ± 900)	-	(19000 ± 2000)	(2200 ± 300)
D (cm ² /s)	0.25	0.44	0.31	0.41
$Q_{\text{TLS}}(10^3)$	(4.33 ± 0.33)	-	(4.34 ± 0.29)	(6.2 ± 0.6)
Q_{other}	-	-	-	-
n_c	(0.013 ± 0.010)	-	(0.011 ± 0.007)	(0.026 ± 0.024)
β	(0.116 ± 0.019)	-	(0.107 ± 0.014)	(0.16 ± 0.04)
$Q_i^S(10^3)$	(3.76 ± 0.08)	(2.33 ± 0.06)	(3.73 ± 0.07)	(4.78 ± 0.08)
Δ_S	(0.071 ± 0.015)	(0.085 ± 0.012)	(0.084 ± 0.013)	(0.065 ± 0.011)
	Si + SiO ₂ + NbTiN+Al ₂ O ₃			
	resonator #13	resonator #14	resonator #15	resonator #16
f_r (GHz)	3.765	5.231	5.474	5.652
$L_k^{\text{sq,rf}}$ (pH)	60	73	61	51
Q_c	(4500 ± 330)	(130000 ± 20000)	(14000 ± 2000)	(2200 ± 200)
D (cm ² /s)	1.22	0.15	0.22	0.33
$Q_{\text{TLS}}(10^3)$	(4.13 ± 0.32)	(5.0 ± 0.5)	(4.93 ± 0.223)	(10.9 ± 0.7)
$Q_{\text{other}}(10^4)$	-	-	-	(5.1 ± 0.5)
n_c	(0.41 ± 0.32)	(1.1 ± 1.0)	(0.36 ± 0.14)	(3.0 ± 1.9)
β	(0.152 ± 0.032)	(0.119 ± 0.029)	(0.118 ± 0.013)	(0.81 ± 0.26)
$Q_i^S(10^3)$	(3.81 ± 0.05)	(1.07 ± 0.11)	(2.93 ± 0.04)	(4.11 ± 0.10)
Δ_S	(0.062 ± 0.009)	(0.15 ± 0.05)	(0.081 ± 0.011)	(0.119 ± 0.022)

TABLE III. **Parameters for all 16 resonators** The shown parameters are the resonance frequency f_r , the sheet kinetic inductance $L_k^{\text{sq,rf}}$, the coupling Q factor Q_c , the diffusion constant D , the low-power internal Q factor Q_{TLS} . n_c is the critical photon number and β the scaling parameter from Eq. (3). Q_i^S is the internal Q factor on resonance with the paramagnetic impurities (compare Fig. 4(a)) and Δ_S is the width of this resonance. Values are missing where the data could not be extracted.